Chapter 1

Introduction

Abstract

This introductory chapter attempts to portray the goal of this thesis from a broad astrophysical perspective. Starting with the motivation of gauging the dark matter mass power-spectrum of early-type galaxies within the ΛCDM paradigm using strong galaxy-galaxy lenses (Section 1.1 – 1.2); this chapter recapitulates the fundamentals of gravitational lensing and surface brightness anomalies (Section 1.3 – 1.6). A description of the state-of-the-art hydrodynamic N-body simulations, i.e. "Evolution and Assembly of GaLaxies and their Environment" (EAGLE), are briefly presented in Section 1.7. These simulations are used in Chapter 6 of this thesis. In Chapter 2 and Chapters 4, 5 of this thesis, observational data from Kilo-Degree Survey (KiDS) and *Hubble Space Telescope* (*HST*) are used, respectively. Short descriptions of these surveys are also presented in Section 1.7. Finally, the mathematical definitions of the power spectrum and two-point correlation function are given in Section 1.8. These statistical instruments have been extensively used in the subsequent Chapters to (i) analyse the strong gravitationally lensed images in order to quantify the matter distribution in the inner regions (1-10 kpc scales) of massive early-type galaxies (Chapters 3 and 4), and (ii) to infer the imprints of various galaxy formation processes, e.g., stellar and AGN feedback, the viscosity of baryonic gas etc., on the mass maps of galaxies (Chapter 6).

1.1 ΛCDM paradigm and missing satellite problem

Dark energy (Λ) plus Cold Dark Matter (ΛCDM) cosmological paradigm predicts that the total mass-energy of the universe contains only 5% visible matter and energy; 27% dark matter and 68% dark energy. So, dark matter constitutes 85% of the total mass, while dark energy and dark matter together constitute 95% of the total mass-energy content of the universe. From the primordial density fluctuations, the dark matter structures form hierarchically, via merging and clustering, from smaller to the more massive ones, which create gravitational potential wells for the interstellar gas to cool down, collapse and ultimately form stars and galaxies. Although this cosmological concordance model successfully reproduces the observed large-scale structures of the universe ($\sim$ 1 Mpc) (Vogelsberger et al. 2014), on smaller sub-galactic and galactic scales, the theoretical predictions and the observations diverge significantly (Bullock & Boylan-Kolchin 2017). For example, the predicted number of substructures in galactic haloes from ΛCDM-based numerical simulations (Klypin et al. 1999), is orders of magnitude larger than the observed number of dwarf satellite galaxies, found in the local group. This discrepancy between large-scale structure simulation and cosmological observations is known as Missing Satellites Problem (MSP) Moore et al. (1999); Diemand et al. (2007); Nierenberg et al. (2016); Dooley et al. (2017).

Three distinct solutions to the MSP have been suggested in the literature:

1. The CDM paradigm is incomplete: This discrepancy points towards alternative dark-matter models, e.g. dark matter with a higher thermal velocity dispersion in the early universe (warm) or self-interacting, decaying or even repulsive dark matte, which ultimately all suppresses the formation of low-mass dark matter subhaloes. For studies of Warm Dark Matter (WDM) models, see e.g. Menci et al. (2012), Nierenberg et al. (2013), Viel et al. (2013), Lovell et al. (2014) and Vegetti et al. (2018).

2. Astrophysical observations are incomplete: The predicted abundance of subhaloes are actually right but they are not efficient enough to form stars due to several baryonic processes such as UV reionization, feedback from supernova (SN), AGN feedback, tidal stripping, suppression of gas accretion, star formation etc. Thoul & Weinberg

(1996); Bullock et al. (2000); Somerville & Davé (2015); Sawala et al. (2014); Despali et al. (2018); Kim et al. (2017), and thus remain undetectable.

3. A third alternative interpretation is that the CDM cosmological paradigm is correct and cosmological observations are also complete, but the Local Group happens to be just a statistically biased environment with less abundant substructure, not being a typical representative of the Universe Muller et al. (2018).

So, investigations of the problem of detecting and quantifying the mass (sub)-structures in galactic scales beyond the Local Group, are crucial to test the solutions, as mentioned above, to MSP, and furthermore to solve small-scale discrepancies in ΛCDM cosmological paradigm. Particularly, gauging the mass structure on the scales of 1-10 kpc will pave the way to distinguish between different galaxy-formation scenarios, and also to compare different dark-matter models (e.g. CDM, WDM).

1.2 Strong lensing and galactic mass distributions

One of the most profound predictions of Einstein's general theory of relativity is the deviation of the paths of light rays from straight lines (or null geodesics), in the presence of gravitational fields. While traversing through space-time, these 'wandering' light rays from distant astrophysical sources create distorted and (de)magnified images (e.g., arcs rings or even multiple images), where intervening galaxies or large scale structures located along the line-of-sight act as the gravitation potentials (i.e. lenses) causing the space-time curvature. This phenomenon is called "gravitational lensing" in astronomy and cosmology (Narayan & Bartelmann 1996; Meylan et al. 2006).

Although dark matter does not interact electromagnetically, due to its mass, it interacts gravitationally, and gravitational lensing is used as a probe to indirectly detect and measure its distribution in the galactic and on the larger scales. By measuring the distortions, magnifications, image multiplicities and the surface brightness fluctuations of a background galaxy (i.e. 'source') – lensed by another foreground galaxy (usually termed as the 'lens galaxy') – the total mass distribution in the lens plane (baryonic and dark matter) can be quantified observationally.

In the process of lens modelling, the potential of the total mass distribution is usually assumed to be smooth. Any density inhomogeneities present in the lens plane or along the line-of-sight, however, lead to addtional perturbations in the observed surface-brightness distribution of the lensed images, which in principle can be traced back to the lensing potential. Similarly, individual dark matter sub-halos in the lens galaxy or along the line-of-sight can be detected using these gravitationally-induced surface brightness anomalies, as shown in Koopmans (2005); Vegetti & Koopmans (2009a); Vegetti et al. (2010a,b, 2012); Despali et al. (2018); Vegetti et al. (2018). Additionally, gravitational lensing has proven to be a useful probe to indirectly detect and quantify the dark halo distributions using flux-ratio anomalies in multiply imaged lensed quasars (Mao & Schneider 1998; Metcalf & Madau 2001; Dalal & Kochanek 2002; Nierenberg et al. 2014; Gilman et al. 2018).

Although the 'gravitational imaging' technique developed by Koopmans (2005); Vegetti & Koopmans (2009a) can account for individual massive subhalos, this formalism cannot be used to detect and quantify the smaller mass-density fluctuations present in the galactic halos. In recent years there has been a considerable number of theoretical studies to address this question, e.g. Bus (2012), Hezaveh et al. (2016a); Diaz Rivero et al. (2018), who have independently proposed statistical solutions to the problem. The primary challenge in this respect seems to be that, besides the CDM substructures in the lens plane and/or along the line-of-sight, various baryonic processes can also contribute to the observed surface-brightness anomalies, such as mergers, stellar streams or edge-on discs Vegetti et al. (2014); Gilman et al. (2017); Hsueh et al. (2016, 2018, 2017), which are not necessarily incorporated in the smooth lens model.

In this thesis, the primary aim has been to develop a novel statistical formalism that can map these excess surface-brightness fluctuations on to a model of the the total mass perturbations, which might arise from the CDM substructures, line-of-sight halos and/or stellar winds or AGN feedbacks mechanisms etc, in the inner regions of the early-type galaxies (1-10 kpc). The final aim is to apply this formalism to observational data and compare the results with the predictions from state-of-the-art N-body hydrodynamical simulations, EAGLE (Schaye et al. 2015; Schaller et al. 2015; Crain et al. 2015).

1.3 The Born approximation

To determine how much a typical distribution of mass of an astrophysically interesting object deflects light rays that are propagating through spacetime, let us first consider a spherically symmetric gravitating body of mass M. Assuming the impact parameter is much larger than Schwarzchild radius of the object, i.e. $\xi \gg R_s = 2GM/c^2$, the deflection angle is give by (see e.g. Narayan & Bartelmann 1996),

$$\hat{\alpha} = \frac{4GM}{c^2\xi} = 1.75'' \Big(\frac{M}{M_{\rm sun}}\Big)\Big(\frac{\xi}{R_{\rm sun}}\Big)^{-1} \tag{1.1}$$

As long as the condition $\xi >> R_s$ holds, it implies $\hat{\alpha} << 1$.

This result can be generalised for three-dimensional continuous mass distributions with volume density $\rho(r)$ as follows. First we divide the total mass distribution M, into smaller cells of volume dV containing infinitesimal mass $dm = \rho(r)\, dV$. This assumption of replacing extended mass as a sum of point masses is valid locally near the lens plane where general relativity can be approximated by linearised gravity. Also assuming that the deflection angle is small, one can consider the trajectory of light rays as straight lines near the deflecting mass (see Figure 1.1). So, if the direction of propagation of the incoming light rays towards the lens plane is along r_3, the gravitational potential along the deflected trajectory can be approximated by the gravitational potential of the undeflected trajectories. This is called *thin lens approximation* or *Born approximation.*Thus the impact parameter of the light ray with respect to an infinitesimal mass element dm at $(\boldsymbol{\xi_1'}, \boldsymbol{\xi_2'}, r_3)$ becomes $(\boldsymbol{\xi} - \boldsymbol{\xi'})$, which is independent of r_3. So, total deflection angle can be written as,

$$\begin{aligned} \hat{\boldsymbol{\alpha}}(\boldsymbol{\xi}) &= \frac{4G}{c^2} \sum dm(\boldsymbol{\xi_1'}, \boldsymbol{\xi_2'}, r_3') \frac{\boldsymbol{\xi} - \boldsymbol{\xi'}}{|\boldsymbol{\xi} - \boldsymbol{\xi'}|^2}, \\ &= \frac{4G}{c^2} \int d^2\xi' \int dr_3'\ \rho(\boldsymbol{\xi'}, r_3') \frac{\boldsymbol{\xi} - \boldsymbol{\xi'}}{|\boldsymbol{\xi} - \boldsymbol{\xi'}|^2}. \end{aligned} \tag{1.2}$$

If one carries out the r_3 integration in the above equation, a two dimensional surface mass density can be defined as follows

$$\Sigma(\boldsymbol{\xi}) = \int dr_3\ \rho(\boldsymbol{\xi}, r_3) \tag{1.3}$$

In terms of which the vector deflection angle can be expressed as

$$\hat{\boldsymbol{\alpha}}(\boldsymbol{\xi}) = \frac{4G}{c^2} \int d^2\xi' \; \Sigma(\boldsymbol{\xi}') \; \frac{\boldsymbol{\xi} - \boldsymbol{\xi}'}{|\boldsymbol{\xi} - \boldsymbol{\xi}'|^2}. \tag{1.4}$$

1.4 The lens equation

The geometry of gravitational lensing (Figure 1.1), together with the small angle approximation yields Kochanek et al. (2000); Schneider (2003),

$$\frac{\left(\boldsymbol{\eta} + D_{ds}\, \hat{\boldsymbol{\alpha}}(\boldsymbol{\xi})\right)}{D_s} = \frac{\boldsymbol{\xi}}{D_d} = \boldsymbol{\theta}, \tag{1.5}$$

where D_s, D_d, D_{ds} are the angular diameter distances. The above geometrical identity can be re-written as,

$$\boldsymbol{\eta} = \frac{D_s}{D_d}\; \boldsymbol{\xi} - D_{ds}\; \hat{\boldsymbol{\alpha}}(\boldsymbol{\xi}). \tag{1.6}$$

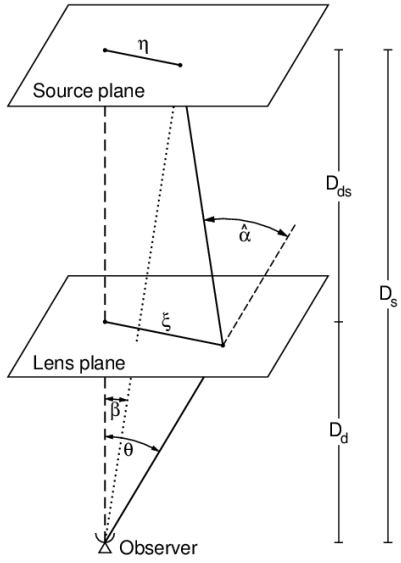

Figure 1.1: The geometry of single lens plane gravitational lensing, source: Schneider (2003)

Using angular coordinates, defined by $\boldsymbol{\eta} = D_s\,\boldsymbol{\beta}$ and $\boldsymbol{\xi} = D_d\,\boldsymbol{\theta}$, we can write the final *lens equation* as,

$$\boldsymbol{\beta} = \boldsymbol{\theta} - \frac{D_{ds}}{D_s}\,\hat{\boldsymbol{\alpha}}(D_d\,\boldsymbol{\theta}) = \boldsymbol{\theta} - \boldsymbol{\alpha}(\boldsymbol{\theta}), \tag{1.7}$$

where the scaled deflection angle $\boldsymbol{\alpha} = \frac{D_{ds}}{D_s}\,\hat{\boldsymbol{\alpha}}(D_d\,\boldsymbol{\theta})$ has been introduced. So, a source with a true angular position $\boldsymbol{\beta}$, at an angular diameter distance D_s from an observer, will be seen at angular positions $\boldsymbol{\theta}$. As the lens equation is non-linear, $\boldsymbol{\theta}$ in this cases has different solutions which gives rise to multiple images of a single source. This is called *strong lensing.*

The lens equation, Equation 1.7 can be made dimensionless by using the so called Einstein radius θ_E which is defined as the radius for which $\boldsymbol{\beta} = 0$. For a spherically symmetric body this value is:

$$\theta_E = \Big(\frac{4GM}{c^2}\frac{D_{ds}}{D_d D_s}\Big)^{1/2} \tag{1.8}$$

We introduce two dimensionless quantities $\mathbf{y} = \boldsymbol{\beta}/\theta_E$ and $\mathbf{x} = \boldsymbol{\theta}/\theta_E$. In this notation lens equation reads as:

$$\mathbf{y}(\mathbf{x}) = \mathbf{x} - \boldsymbol{\alpha}(\mathbf{x}). \tag{1.9}$$

We will use this notation in Chapter 3 to develop the power spectrum formalism. The scaled deflection angle can be expressed in terms of the surface mass density as below

$$\boldsymbol{\alpha}(\boldsymbol{\theta}) = \frac{1}{\pi}\int_{\mathbb{R}^2} d^2\theta'\;\kappa(\boldsymbol{\theta}')\;\frac{\boldsymbol{\theta}-\boldsymbol{\theta}'}{|\boldsymbol{\theta}-\boldsymbol{\theta}'|^2}, \tag{1.10}$$

where the *convergence* or dimensionless surface mass density is defined as

$$\kappa(\boldsymbol{\theta}) = \frac{\Sigma(D_d\boldsymbol{\theta})}{\Sigma_{cr}} \qquad ; \qquad \Sigma_{cr} = \frac{c^2}{4\pi G}\frac{D_s}{D_d\;D_{ds}}. \tag{1.11}$$

The *critical surface mass density* Σ_{cr} gives us a limit of strong or weak lensing. If $\kappa \geq 1$ or $\Sigma \geq \Sigma_{cr}$ we can get multiple images for a single source.

Now using the mathematical identity $\nabla \ln|\boldsymbol{\theta}| = \boldsymbol{\theta}/|\boldsymbol{\theta}|^2$ we can further write the scaled deflection angle as the gradient of a scalar potential,

$$\boldsymbol{\alpha} = \nabla\psi \tag{1.12}$$

where the lensing deflection potential is defined as,

$$\psi(\boldsymbol{\theta}) = \frac{1}{\pi}\int_{\mathbb{R}^2} d^2\theta'\ \kappa(\boldsymbol{\theta}')\ln|\boldsymbol{\theta}-\boldsymbol{\theta}'| \tag{1.13}$$

Also we may write Poisson's equation in two dimensions by using the identity $\nabla^2 \ln|\boldsymbol{\theta}| = 2\pi\delta(\boldsymbol{\theta})$, where $\delta(\boldsymbol{\theta})$ denotes the Dirac delta function,

$$\nabla^2\psi = 2\kappa. \tag{1.14}$$

Both the scaled deflection angle $\boldsymbol{\alpha}$ and the lensing deflection potential ψ, as defined above, are dimensionless.

1.5 Magnification, critical curves & caustics

In gravitational lensing, the shapes of the images differ from the shapes of the sources due to the differential deflection of light bundles, i.e. small areas of the source appear distorted in the lensed images as seen by an observer. If there is no other source or sink of emission or absorption of photons then Liouville's theorem implies that, lensing conserves surface brightness or specific intensity. So, if $I^{(s)}(\boldsymbol{\beta})$ is the surface brightness distribution in the source plane, then the observed surface brightness distribution in the lens plane is

$$I(\boldsymbol{\theta}) = I^{(s)}[\boldsymbol{\beta}(\boldsymbol{\theta})] \tag{1.15}$$

The distortion of infinitesimally small images can be described by the Jacobian matrix,

$$A(\boldsymbol{\theta}) = \frac{\partial\boldsymbol{\beta}}{\partial\boldsymbol{\theta}} = \Big(\delta_{ij} - \frac{\partial^2\psi(\boldsymbol{\theta})}{\partial\theta_i\partial\theta_j}\Big) = \begin{pmatrix} 1-\kappa-\gamma_1 & -\gamma_2 \\ -\gamma_2 & 1-\kappa+\gamma_1 \end{pmatrix} \tag{1.16}$$

where we have introduced the complex *shear* $\gamma = \gamma_1 + i\gamma_2 = |\gamma|e^{2i\phi}$ with components,

$$\gamma_1 = \frac{1}{2}(\psi_{,11} - \psi_{,22}), \qquad \gamma_2 = \psi_{,12} \tag{1.17}$$

In terms of dimensionless notation, the elements of the Jacobian matrix can be written as,

$$A_{ij} = \frac{\partial y_i}{\partial x_j} = \Big(\delta_{ij} - \frac{\partial^2\psi(x)}{\partial x_i\partial x_j}\Big). \tag{1.18}$$

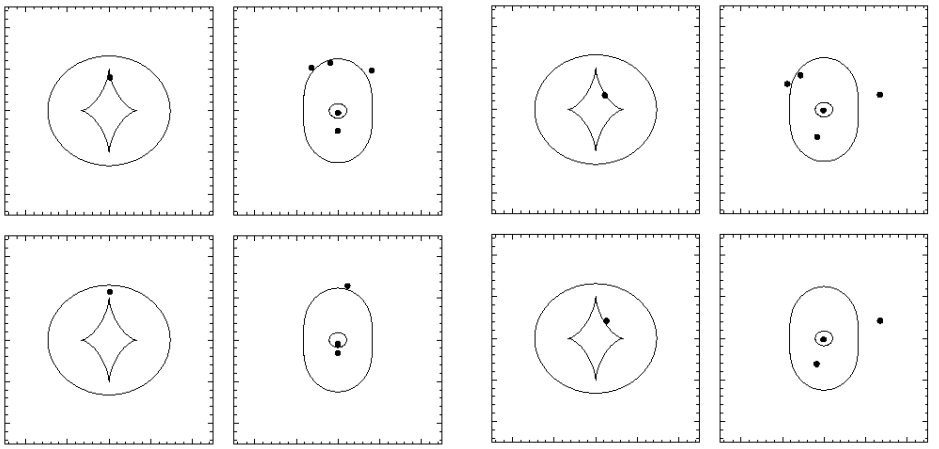

Cusp configuration in the source plane, producing a long axis quad and a double.

Fold configuration of the source, leading to an inclined quad and a double.

Figure 1.2: Caustics and critical curves for a cusp (left 2×2 panel) and fold (right 2×2 panel) configurations. Notice that, as the source crosses the diamond caustic (from inward to outwards), two lensed images merge on the tangential critical line and then disappear. Source: Courbin et al. (2002)

If $\boldsymbol{\theta_0}$ is a point in the image plane corresponding to a point $\boldsymbol{\beta_0}$ in the source plane, we can write to first order Taylor expansion,

$$\begin{aligned} I(\boldsymbol{\theta}) &= I^{(s)}[\boldsymbol{\beta_0} + \Big(\frac{\partial \boldsymbol{\beta}}{\partial \boldsymbol{\theta}}\Big)_{\boldsymbol{\theta}=\boldsymbol{\theta_0}} \cdot (\boldsymbol{\theta} - \boldsymbol{\theta_0})] \\ &= I^{(s)}[\boldsymbol{\beta_0} + A(\boldsymbol{\theta_0}) \cdot (\boldsymbol{\theta} - \boldsymbol{\theta_0})], \end{aligned} \tag{1.19}$$

which shows us that circular sources become elliptical images, where the ratios of semi-axes of the image to the radius of the source are given by $(1 - \kappa \pm |\gamma|)^{-1}$.

The magnification matrix M is determined by the inverse of the Jacobian A,

$$M = A^{-1} = \frac{\partial \mathbf{x}}{\partial \mathbf{y}}. \tag{1.20}$$

The magnification $|\mu(\boldsymbol{\theta_0})|$ is defined as the ratio of the areas observed from the image and from the unlensed source assuming the surface brightness is

constant inside a small area. This is given by the ratio of the integrals over $I(\theta)$ and $I^{(s)}(\beta)$ which is same as the determinant of magnification tensor,

$$\mu = \mathbf{det}\ M = \frac{1}{\mathbf{det}\ A} = \frac{1}{(1-\kappa)^2 - |\gamma|^2}. \tag{1.21}$$

The total magnification is the sum over magnifications over all the images:

$$\mu_p(\boldsymbol{\beta}) = \sum_i\ |\mu(\boldsymbol{\theta_i})|. \tag{1.22}$$

The magnification of a real source with finite extent is then given by weighted mean of μ_p over the source's area,

$$\mu = \frac{\int d^2\beta\ I^{(s)}(\boldsymbol{\beta})\ \mu_p(\boldsymbol{\beta})}{\int d^2\beta\ I^{(s)}(\boldsymbol{\beta})}. \tag{1.23}$$

Finally critical curves are closed smooth curves in the lens plane for which $\mathbf{det}\ A(\boldsymbol{\theta}) = 0$. So, magnification $\mu = 1/\mathbf{det}\ A$ diverges for an image on the critical curve. If we map these critical curves on the source plane via lens equation, we get caustics. Caustics may not necessarily be smooth and can have cusps. The regions delimited by the caustics define the multiplicity of the strong lens. A source crossing a caustic will either create or destroy two lensed images (see Figure 1.2).

1.6 Surface brightness anomalies

If the surface brightness of the source and the image are denoted by $S(\mathbf{y})$ and $I(\mathbf{x})$ respectively, according to the principle of conservation of surface brightness in gravitational lensing,

$$S(\mathbf{y}) = I(\mathbf{x}) \tag{1.24}$$

where $\mathbf{y}$ and $\mathbf{x}$ are chosen coordinates in the source and in the lens plane, respectively. Inserting the lens equation in this relation we get,

$$I(\mathbf{x}) = S(\mathbf{x} - \boldsymbol{\alpha}) = S(\mathbf{x} - \nabla\psi(\mathbf{x}). \tag{1.25}$$

The non-linear lens equation (Equation 1.9) together with conservation of surface brightness (Equation 1.24), are the fundamental equations in strong

gravitational lensing for adaptive grid-based Bayesian lens-modelling codes, e.g. Vegetti & Koopmans (2009a); Koopmans (2005) which has been used in Chapter 4 to model HST lenses and, which simultaneously reconstruct both the *unknown* lensing potential $\psi(\mathbf{x})$ and the *unknown* surface-brightness distribution of the background source $S(\mathbf{y})$, from the *known* observed surface brightness of the lensed image $I(\mathbf{x})$. These two above equations also form the basis of the theory that is developed in Chapter 3 (Chatterjee & Koopmans 2018).

In strong lensing terminology, a smooth lens model of the lensing potential ψ_0, is defined as a potential which can be expressed in terms

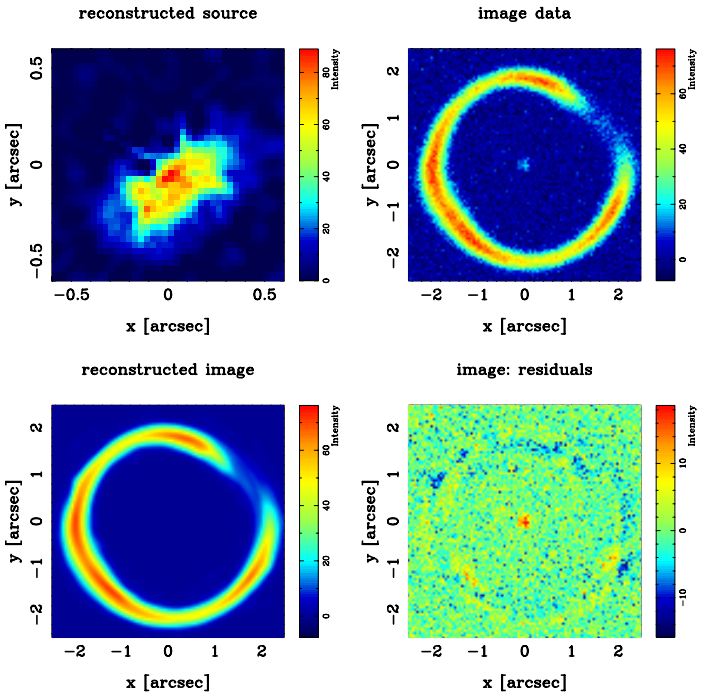

Figure 1.3: An example of strong gravitational lens and source modelling. Upper-right corner shows a simulated noisy image data which is modelled using CAULDRON code to reconstruct the source (upper-left) and the smooth model (lower-left). The difference between the *true* image data and the reconstructed model, is shown as image residuals. Source: Barnabè et al. (2009)

of a small set of parameters (typically $\sim$ 10) and which we obtain by modelling the surface brightness of the observed lens images $I(\mathbf{x})$. This can be performed by either via grid-based adaptive modelling or by a parametric modelling. This leads to a so-called "smooth model" of the lensed image $I_0(\mathbf{x})$. The residuals (or a surface-brightness difference $\delta I(\boldsymbol{x})$ between the observed and the modelled lens galaxy) are then written as

$$\delta I(\boldsymbol{x}) = I(\boldsymbol{x}) - I_0(\boldsymbol{x}) = S(\boldsymbol{x} - \nabla\psi(\boldsymbol{x})) - S(\boldsymbol{x} - \nabla\psi_0(\boldsymbol{x})). \qquad (1.26)$$

In galaxy-galaxy strong lensing, we refer to such surface-brightness discrepancies $\delta I(\boldsymbol{x})$, caused by the perturbation of the true lensing potential $\psi(\boldsymbol{x})$ from the best-fitting smooth lensing potential $\psi_0(\boldsymbol{x})$, as *surface-brightness anomalies* (see for example Figure 1.3). We attempt to describe these surface brightness anomalies statistically since they are often not easy to model or describable by a limited set of parameters. We connect these surface-brightness anomalies to the total lens potential fluctuations (baryonic plus dark matter), through describing these perturbations as a random field, and furthermore via estimating the properties/parameters of this random field from observed gravitational lenses and cosmological simulations.

1.7 EAGLE, KiDS, HST – simulations & observations

In the next two subsections, a brief description of the EAGLE N-body hydrodynamical simulations and the HST and KiDS surveys are given.

EAGLE

In order to study various galaxy-formation processes e.g. mergers, collapse, accretions, feedbacks and their imprints on the mass distribution of the galaxies, relatively large samples of two dimensional projected mass-maps of early-type elliptical galaxies, corresponding to nine different galaxy formation scenarios from "Evolution and Assembly of GaLaxies and their Environment" (EAGLE) hydrodynamic N-body simulations have been used in this thesis. Emphasising the importance of cosmological simulations in astronomy, Joop Schaye writes,

> *"Simulations enable astronomers to "turn the knobs" much as experimental physicists are able to in the laboratory."* (Schaye et al. 2015)

Within the standard ΛCDM universe, EAGLE simulation follows a hydrodynamic prescription towards the formation of galaxies and supermassive black holes in cosmologically representative volumes (e.g. box sizes of 50-100 cMpc). Four out of nine EAGLE galaxy-formation models that are used in this thesis were calibrated to reproduce the observed Galaxy Stellar Mass Function (GSMF) at $z = 0.1$, implementing different star formation feedback processes in its sub-grid physics. EAGLE also incorporates black hole growth via adopting accretion, merger and AGN feedback schemes in the N-body simulations. The subgrid physical parameters, such as the viscosity of accretion disks or temperature increment due to AGN heating, are incorporated as "tuning" parameters of the simulations. One notable feature of EAGLE simulation is, how the feedback from the massive stars and the AGNs are implemented, via injection of stochastic thermal energy into the ISM without the need of turning off the cooling or, decoupling the hydrodynamical forces. The feedback efficiencies are set from the calibration with currently established galaxy stellar mass function, and from the galaxy-central black hole mass relation; also incorporating the galaxy sizes. The results from EAGLE simulations find good agreement with observed Tully-Fisher relation, star formation rates, total stellar luminosities of galaxy clusters etc. For more details on the model variations and the sub-grid physics, see Schaye et al. (2015); Schaller et al. (2015); Crain et al. (2015); Mukherjee et al. (2018a) and Section 6.2 of this thesis.

Kilo Degree Survey (KiDS)

The Kilo-Degree Survey (KiDS) is a 1500 square degree extra-galactic optical imaging survey, in four optical bands (*u, g, r* and *i*, de Jong et al. 2015) carried out using the OmegaCAM wide-field imager (Kuijken 2011). It is mounted at the Cassegrain focus of the 2.6m VLT Survey Telescope (VST) at Paranal Observatory in Chile. Median PSF FWHM values in *u, g, r* and *i* are 1.0, 0.8, 0.65 and 0.85 arcsec, respectively. Although primarily this survey was designed for dark-matter studies at cosmological scale via weak lensing, high image quality and wide surveying area make KiDS data particularly suitable for strong lensing as well. A Luminous Red Galaxy sample (LRGs, Eisenstein et al. 2001) selected from 255 square degrees of the KiDS-ESO data release 3 (DR3) has been used to build the training set for the Convolutional Neural Network (CNN, see Chapter 2), in order

to find the strong gravitational lens candidates in KiDS. For more details see Petrillo et al. (2017, 2018).

Hubble Space Telescope (HST)

Besides the Compton Gamma Ray Observatory, the Spitzer Space Telescope and the Chandra X-ray Observatory, Hubble Space Telescope (HST) is one of the NASA's *Great Observatories*, named after the astronomer Edwin Hubble. HST has been in operation since 1990. With a 2.4-meter mirror, HST mostly observes in the near ultraviolet (UV), visible, and near infrared (IR) spectra. In Chapter 4 HST-imaging (using U band, WFC3/F390W filter) of SDSS J0252+0039 – one of the ten U-band observed galaxy-galaxy strong gravitational lens candidates from the SLACS Survey – has been used to give observational constraints on total sub-galactic mass-fluctuations. The latter could arise from various baryonic processes as well as from small-sized dark matter subhalo distributions present on the lens plane, and/or along the line of sight. For a more detailed description of the HST data of this lens system, see Bayer et al. (2018).

1.8 The power-spectrum and correlation functions

On the angular scales of strong lensing, one can apply the flat sky approximation, and Fourier transform the image surface brightness as follows

$$\begin{aligned} I(\mathbf{x}) &= \int \frac{\mathrm{d}^2\mathbf{k}}{2\pi} I(\mathbf{k}) e^{i\mathbf{k}\cdot\mathbf{x}}, \\ I(\mathbf{k}) &= \int \frac{\mathrm{d}^2\mathbf{x}}{2\pi} I(\mathbf{x}) e^{-i\mathbf{k}\cdot\mathbf{x}}. \end{aligned} \tag{1.27}$$

If we assume that the surface brightness anomalies of the image are statistically isotropic,[1] the real-space two-point correlation function ξ of the surface brightness only depends on the separation between the two points,

$$\langle I(\mathbf{x}) I(\mathbf{x}') \rangle = \xi^{II}(|\mathbf{x} - \mathbf{x}'|). \tag{1.28}$$

[1] Which might not hold for a single lens, but for an ensemble of lenses, it will.

With this assumption, the covariance of the Fourier components of the surface brightness is

$$\begin{aligned}\langle I(\mathbf{k})I^*(\mathbf{k}')\rangle &= \int \frac{\mathrm{d}^2\mathbf{x}}{2\pi} \int \frac{\mathrm{d}^2\mathbf{x}'}{2\pi}\, e^{-i\mathbf{k}\cdot\mathbf{x}} e^{i\mathbf{k}'\cdot\mathbf{x}'} \xi^{II}(|\mathbf{x}-\mathbf{x}'|) \\ &= \int \frac{\mathrm{d}^2\mathbf{x}}{2\pi} \int \frac{\mathrm{d}^2\mathbf{r}}{2\pi}\, e^{i(\mathbf{k}'-\mathbf{k})\cdot\mathbf{x}} e^{i\mathbf{k}'\cdot\mathbf{r}} \xi^{II}(r) \\ &= \delta(\mathbf{k}'-\mathbf{k}) \int \mathrm{d}^2\mathbf{r} e^{i\mathbf{k}\cdot\mathbf{r}} \xi^{II}(r). \end{aligned} \tag{1.29}$$

In the second line we changed variables to $\mathbf{r} = \mathbf{x} - \mathbf{x}'$ and then $\mathbf{r} \to -\mathbf{r}$, and have defined $r \equiv |\mathbf{r}|$, which is the correlation length in image plane. The power spectrum of the surface brightness field of source is therefore diagonal in $\mathbf{k}$, and given by

$$\langle I(\mathbf{k})I^*(\mathbf{k}')\rangle = P_k^{II}\delta(\mathbf{k}-\mathbf{k}'). \tag{1.30}$$

where we have defined the power spectrum P_k^{II} as follows,

$$P_k^{II} \equiv \int \mathrm{d}^2\mathbf{r} e^{i\mathbf{k}\cdot\mathbf{r}} \xi^{II}(r). \tag{1.31}$$

In the statistical formalism that is developed in Chapter 3, the power spectrum and two-point correlation functions are used as statistical measures to describe the surface brightness fluctuations in the lensed images and to quantify its correlation with that of the source and the potential perturbations in the lens plane.

1.8.1 Hankel transform

Because of the axi-symmetry of the problem, the Fourier Transform can be simplified further. If we use the following expansion of $e^{i\mathbf{k}\cdot\mathbf{r}}$ into Bessel functions $J_n(r)$

$$\begin{aligned} e^{ikr\cos\phi} &= \sum_{n=-\infty}^{\infty} i^n J_n(kr) e^{in\phi} \\ &= J_0(kr) + 2\sum_{n=1}^{\infty} i^n J_n(kr)\cos(n\phi), \end{aligned} \tag{1.32}$$

and then if we integrate over ϕ, the only term that remains is $J_0(r)$. This makes the Fourier transform as a Hankel transform which allows us to write

the power spectrum as follows,

$$\begin{aligned} P_k^{II} &= \int \mathrm{d}^2\mathbf{r} e^{i\mathbf{k}\cdot\mathbf{r}} \xi^{II}(r) \\ &= \int r\mathrm{d}r \int \mathrm{d}\phi_{\mathbf{r}}\, e^{ikr\cos(\phi_{\mathbf{k}}-\phi_{\mathbf{r}})} \xi^{II}(r) \\ &= 2\pi \int r\mathrm{d}r\, J_0(kr)\xi^{II}(r). \end{aligned} \tag{1.33}$$

We use this in Chapter 2.

1.9 This thesis

Some of the questions critical to strong gravitational lensing, which are investigated in this thesis are,

1. How can one statistically quantify the surface brightness anomalies (as described in Section 1.6) for a large sample of lens galaxies using a power spectrum formalism, assuming that they originate from the lens potential fluctuations?

2. How much degeneracy is there causing some of the surface brightness residuals in lensed images – that arise from the lens potential fluctuations – to get absorbed in the reconstructed source surface brightness during the Bayesian modelling, given that both ψ_0 and $S(\mathbf{y})$ are unknown?

3. Can there be any other systematic dependencies and bias in the adaptive grid-based Bayesian source and lens reconstruction, besides the above-mentioned degeneracy?

In this thesis, I develop a novel statistical approach to answer the first question, by quantifying the mass power-spectrum on 1-10 kpc scales of early-type galaxies (**Chapter 3**). I contribute to connecting this theoretical framework to HST observations in **Chapter 4**, and I compare these to numerical hydrodynamic simulations in **Chapter 6**. In **Chapter 5**, I perform various systematic tests in order to gauge the biases and degeneracies in the Bayesian adaptive grid-based lens modelling that we use to model these lenses and investigate questions 2 and 3. Part of the formalism and simulation results that have been developed have also been applied to create the mock training sets in machine learning (Convolutional

Neural Network, CNN), These CNNs were trained to find gravitational lens systems from Kilo-Degree Survey (KiDS) data (**Chapter 2**). For each chapter, I describe the research and contribution that I made to the referenced papers.

In more detail, the thesis is structured as follows:

(a) **Chapter 2** describes the simulations and lens models that I have developed to

- train convolutional neural networks to find strong lens candidates from KiDS survey (Chapter 2),
- verify the theoretical framework of Chapter 3,
- and to the HST observations (Chapter 4, 5).

Primarily the Non-singular Isothermal Ellipsoid lens model (NIE) is used as a smooth lens potential, where Gaussian Random field fluctuations were added on top of the lens potential as potential perturbations. Details of the simulations of different realisations and their effects on the surface brightness fluctuations of strong lenses are presented in that chapter. The chapter ends with a listing of some of the typical images of the lens candidates that have been found from the KiDS survey using our CNN.

(b) **Chapter 3** is a theoretical proof-of-concept chapter. It presents a new statistical framework to quantify the power spectrum of the surface brightness fluctuations in galaxy-galaxy strong lensed images, and connect it to the lens potential perturbations, assumed they originate from small-scale fluctuations in the potential (Chatterjee & Koopmans 2018). Some tests on typical simulated mock lenses are also presented as verifications of the methodology.

(c) **Chapter 4** represents the applications of the simulations and statistical formalism, as described in Chapter 2, 3, to observational data. This chapter is an outcome of collaboration with D. Bayer, on lens systems of Sloan Lens ACS (SLACS) Survey: SDSS J0252+0039. The inferred power spectrum of the image residuals (after subtracting the best lens model) from this gravitational lens system – modelled by a Bayesian grid-based code (Vegetti & Koopmans (2009a)) – has

been used as an observational upper limit to constrain the parameters of the lens-potential fluctuations. The latter are assumed to be a Gaussian random field as a first-order approximation (for details see Bayer et al. 2018).

(d) **Chapter 5** represents the first results from a collaboration with G. Vernardos on the double lens system SDSSJ0946+1006, which has been modelled using a new grid-based adaptive Bayesian lens modelling code (for details see Vernardos et al., in prep). Using the power spectrum as a probe, this strong gravitational lens system has been used to analyse and quantify the degeneracies and biases in the Bayesian lens modelling.

(e) **Chapter 6** presents the power spectrum analysis of simulated galaxies, corresponding to nine different galaxy evolution scenarios obtained from the state-of-the-art EAGLE N-body hydrodynamic simulations (Schaye et al. 2015; Schaller et al. 2015; Crain et al. 2015). We analyse the normalised mass maps of these massive early-type elliptical galaxies and try to infer the effects of hitherto physical processes, like stellar and AGN feedback, and the environment, like viscosity, metallicity, density etc., in their mass distribution using a power-spectrum formalism. This chapter soon paves the way to compare the observational upper limits with the simulation scenarios to gain better insight regarding galaxy formation and evolution mechanisms.

(f) **Chapter 7** concludes the thesis by summarising the key results from five scientific Chapters, along with some insights on the prospects of this work.